We are IntechOpen, the world's leading publisher of Open Access books Built by scientists, for scientists

6,900
Open access books available

185,000
International authors and editors

200M
Downloads

Our authors are among the

154
Countries delivered to

TOP 1%
most cited scientists

12.2%
Contributors from top 500 universities



WEB OF SCIENCE™

Selection of our books indexed in the Book Citation Index in Web of Science™ Core Collection (BKCI)

Interested in publishing with us?
Contact book.department@intechopen.com

Numbers displayed above are based on latest data collected.
For more information visit www.intechopen.com



12

Recent Advances in Synthetic Aperture Radar Enhancement and Information Extraction

Dušan Gleich and Žarko Čučej
University in Maribor, Faculty of Electrical Engineering and Computer Science, Maribor Slovenia

1. Introduction

Synthetic Aperture Radar (SAR) systems are all-weather, night and day, imaging systems. Automatic interpretation of information in SAR images is very difficult because SAR images are affected by a noise-like characteristic called *speckle* that arises from an imaging device and strongly data and makes automatic image interpretation very difficult. The speckle noise in SAR images can be removed using an image restoration technique called despeckling. The goal of despeckling is to remove speckle-noise from SAR images and to preserve all image's textural features. The statistical modeling of SAR images has been intensively investigated over recent years. In statistical image processing an image can be viewed as the realization of a joint probability density function. Since joint probability functions have analytical forms and few unknown parameters usually, the efficiency of the denoising algorithm depends on how well the chosen model approximates real data.
The wavelet Daubechies (1992) based despeckling algorithms are proposed in Dai et al. (2004), Argenti et al. (2006), Foucher et al. (2001). The second-generation wavelets like Contourlet Chuna et al. (2006) have appeared over the past few years. Despeckling using Contourlet transform Li et al. (2006) and Bandelet Sveinsson & Benediktsson (2007) transforms show superior despeckling results for SAR images compared with the wavelet based methods. Model based despeckling mainly depends on the chosen models. Bayesian methods have been commonly used as denoising methods, where the prior, posterior and evidence probability density functions are modeled. The image and noise models in the wavelet domain are well-defined using the results in Argenti et al. (2006), Gleich & Datcu (2007) and the noise free image is estimated using a MAP estimate. The speckle noise in the SAR images is considered as a multiplicative noise Walessa & Datcu (2000), and can be also presented as a signal-dependent additive noise Argenti et al. (2006). The log transformed image is modeled using zero location Cauchy and zero-mean Gaussian distributions in order to develop minimum means absolute error estimator, and maximum a posteriori estimator. This paper presents the state-of the art methods for information extraction and their comparison in efficiency of despeckling and information extraction. This paper presents three methods for despeckling and information extraction. The first method is wavelet-based despeckling and information extraction method using the General Gauss-Markov Random Field (GGMRF) and Bayesian inference of first and second order. The second and third methods use the GMRF and Auto-binomial model with the Bayesian inference of first and second order. The despeckling performance is compared and the texture parameters estimation is presented.

2. Synthetic Aperture Radar System

The Synthetic Aperture Radar systems are all weather, day and night monitoring systems, which use the electromagnetic radiation for image retrieval. SAR is one of the most advanced engineering inventions systems in the last decade. Specific radar systems are imaging radars, such as side looking SAR and SAR. Practical restriction to the length of the antenna resulted in very coarse resolution in the flight direction. Using a fixed antenna, illuminating a strip or swath to the sensor's ground track, resulted in the concept of stripping mapping. Modern phased-array antennas are able to perform even more sophisticated data collections strategies, as ScanSAR, spotlight SAR, but the strip map mode is the most applied mode on current satellites [1]. The concept of using frequency (phase) information in the radar signal's along-track spectrum to discriminate two scatters within the antenna beam goes back to 1951 (Carl Wiley). The key factor is coherent radar,, where the phase and amplitude are received and preserved for later processing., but long antenna was required. The early SAR systems were based on optical processing of the measured echoed signal using the Fresnel approximation for image formation and are known as range-Doppler Imaging or polar format processing. The experience on airborne SAR systems in 60's and 70's culminated in L-band SAR system Seasat, a satellite launched in June 1978, primarily for ocean studies, the live time was 100 days, but the imaginary was spectacular, highlighting if geologic information and ocean topography information. Since 1981 Shuttle missions carried SAR systems. The first instrument was the Shuttle Imaging radar SIR laboratory and operated for 2.5 days. An improved version of SIRA orbited the Earth in 1984 and was able to steer the antenna mechanically to enable different angels. Cosmos 1870 was the first S-band SAR satellite of former Soviet Union, launched in 1987 and orbited at a height of 270 km and operated for 2 years, ALMAZ-1 was the second satellite launched in 1991 and operated for 1.5 years. First European Remote Sensing Satellite ERS-1 was operational in 1991 and operated until March 2000. Japan started space-borne SAR program in 1992 with JERS in 1992, SIR-C/X-SAR was developed by JPL, DLR and ASI operated with C, L and X band. Canadian Space Agency lunched Radarsat in 1995. A SRTM (Shuttle Radar Topography mission) was carried out between 11 and 23 February 2000. In last decade many other satellites with SAR were lunched: Radarsat-2, ENVISAT, TerraSAR-X, Tandem-X, ALOS, Cosmo-Skymed, SAR lupe and forth coming constellation of Sentinel satellites.

2.1 Principles of SAR

The central idea of SAR processing is based upon matched filtering of the received signal in both the range and azimuth directions. Matched filtering is possible because the acquired SAR data are modulated in these directions with appropriate phase functions. The modulation in range is provided by the phase encoding of transmitted pulse, while the modulation in azimuth is created by the motion in the signal. The point targets are arrayed in a Cartesian type Coordinate system space defined by range, azimuth, and altitude as analogs of x, y and z directions. The altitude direction is omitted in the two-dimensional simulation. The platform in this simulation is an antenna attached to a plane traveling at an orbital velocity, along the azimuth direction and at the midpoint in the flight, the distance to the target equals the range of closest approach or minimum range to target. As an satellite platform is used in the simulation, the curvature of the earth is considered negligible and the orbital velocity is approximately equal to the platform velocity. The transmitted radar signal, $x(t)$, is assumed to be a chirp pulse (linearly frequency modulated signal) given by

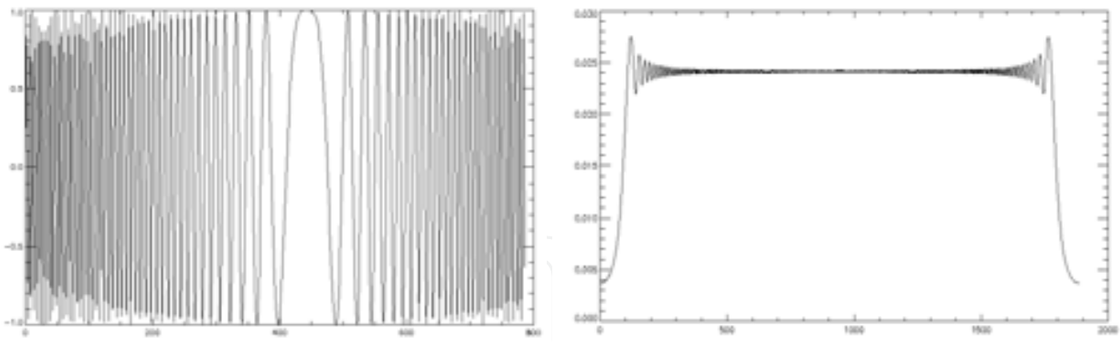


Fig. 1. Chirp signal (left) and its Fourier transform (right).

$$rec\left(\frac{t}{T_r}\right)cos(2\pi f_0 + \pi K_r t^2) \tag{1}$$

where $f_0 = 9.63GHz$, pulse duration $T_r = 25\mu s$, (frequency bandwidth of the chirp=300MHz), K_r is range of the FM rate, measured $MHz/\mu s$. The chirp signal in time domain and its impulse response and its Fourier transform are shown in Fig. 1.

The transmitted radar signal as a cosine with a linearly ramping up frequency over a transmit duration followed by a null receive duration. The transmit window is called the pulse envelope, and defines the duration of the transmission. During the receive duration, the antenna waits to receive reflected radar signals from the targets contained in a one-dimensional range slice echo as function of quick time. One over the combined transmit and receive duration is called the pulse repetition frequency, PRF, and defines the amount of pulses transmitted per second.

The chirp signal is complex and has a complex envelope $g(t)$

$$x(t) = g(t)\exp(j2\pi f_0 \tau) \tag{2}$$

Let a point scatterer has a dimension, smaller then the wavelength $\lambda = c/\nu_0$ be located at a distance R - range away from the radar. The radar platform has a velocity v. The point is seen at the elevation angle and azimuth angle from the antenna main pointing direction. The received echo is proportional to the transmitted wave and delayed by the round-trip delay $2R/c$. In the receiver the echo signal is coherently demodulated, i.e. carrier frequency is removed, resulting echo signal of the point scatterer. The phase term depends on R, governs the interference of echoes from different scatterers. The shape of the pulse envelope $g(\tau)$ determines the range resolution of the radar, it is the ability of radar to distinguish two scatterers at slightly different ranges. $g(\tau) = sinc(\tau B)$. The achievable range resolution defined as half power width of $g(\tau)$.

$$R = 0.885\frac{c}{2B_0} \tag{3}$$

The chirp functions can be compressed to a sinc function by correlation with a chirp function with the same frequency rate, thus leading to the resolution. This so-called range compression is often the first step in SAR data processing. The only relevant parameter

influencing on range resolution is range pulse bandwidth. In range only one pulse was considered for explanation. As the sensor advances along its path, subsequent pulses are transmitted and received by radar. The pulses are transmitted every 1/PRF (pulse repartition frequency). The target is illuminated by many pulses. The strength of each pulse varies, primarily because of the azimuth beam pattern. The signal strength decreases until target lies in the first null of the pattern beam. The energy in outside the main beam contributes to the azimuth ambiguities in the processed image. The received signal has the same waveform as transmitted signal, but it is much weaker and has a frequency shift governed by the relative speed of the sensor and the scatterer. If the distance between target and antenna is decreasing, the frequency of the received signal decreases. This effect is called SAR Doppler frequency. The received signal from the target consists of several parameters, which depicts azimuth chirp and range migration effect. The received signal consists of (i) amplitude range dependence and the elevation antenna pattern, (ii) part which reflects 2-way antenna pattern of the sensor, which represents the synthetic aperture length and is proportional to range r0, (iii) echo signal envelope and its position in fast time, (iv) the factor, which translates the range trajectory of the point scatterer into a phase history, it is called azimuth chirp and its frequency is given by

$$f_D = \frac{1}{2\pi}\frac{d}{dt}\phi(t-t_0) = -\frac{2}{\lambda}\frac{v^2}{r_0}(t-t_0) \tag{4}$$

It is also called Doppler frequency. The Doppler frequency at the beam center is Doppler Centroid f_{DC}

$$f_{DC} = f_D(t-t_c) = FMt_c \tag{5}$$

Where FM is frequency modulation rate of the azimuth chirp. The FM rate is always negative.

$$FM = -\frac{2}{\lambda}\frac{v^2}{r_0} \tag{6}$$

The azimuth resolution is given by

$$A = \frac{0.866v\cos\theta}{f_{DC}} \approx \frac{L}{2} \tag{7}$$

The azimuth resolution is independent of range, velocity or wavelength. The actual resolution is a function of how much of the bandwidth is processed and the combined shape of the beam pattern and the weighting function. The received and demodulated radar signal is referred to as the SAR signal space as it is still in its raw form and the two-dimensional image of the magnitude of the two-dimensional imaginary signal would not allow recognition of targets.

2.2 Range Migration algorithm

The range Doppler algorithm (RDA) was developed in 1976-1978 for processing SEASAT SAR data. Later it was used to digitally process space borne SAR image in 1978 and it is still the most widely used algorithm today. RDA operates in range and azimuth frequency domain, but it has the simplicity of one-dimensional operations. The reflected energy from

areas on the earth's surface in the same range but in different azimuth, are located on the same azimuth frequency. So, when this frequency is adjusted, the whole target areas with the same frequency (which means in the same range) are adjusted. RDA uses the large difference in time scale of range and azimuth data and approximately separates processing in these two directions using Range Cell Migration Correction (RCMC). RCMC is the most important part of this algorithm. RCMC is performed in range frequency and azimuth frequency domain. Since, azimuth frequency is affected by Doppler Effect and azimuth frequency is bonded with Doppler frequency, it is called Range Doppler Algorithm. RDA can be implemented in three different ways. But they all have similar steps and their difference is only in Secondary Range Compression (SRC). The main steps of RDA are: 1- Range compression 2- Azimuth FFT (transform to range Doppler domain) 3- RCMC 4- Azimuth filtering 5- Inverse FFT (return to range azimuth time domain) 6- Image formation. Range compression is implemented using matched filter. The filter is generated by taking the complex conjugate if the FFT of the zero padded pulse replica, where the zeros are added to the end of the replica array. The output of the range matched filter is the inverse transform between range Fourier transformed raw data and the frequency domain matched filter. Each azimuth signal is Fourier transformed via an azimuth FFT and RCMC is performed before azimuth matched filtering in the range-Doppler domain. After azimuth matched filtering of each signal and azimuth inverse fast Fourier transforms (IFFTs), the final target image is obtained.

Fig. 2 shows, real and imaginary part of the received signal, The simulated raw data and its real part and phase are shown in Fig. 3. Fig.4 shows the process of range compression with RCMC and its phase.

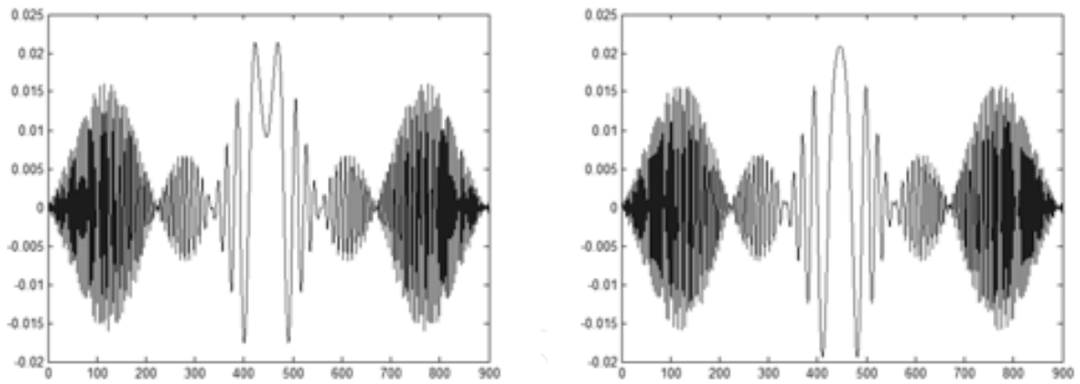


Fig. 2. Real and imaginary part of the received signal.

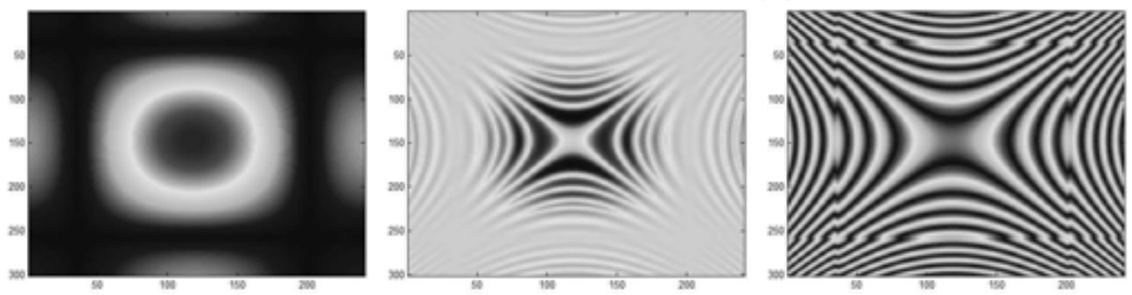


Fig. 3. Simulated SAR raw data: amplitude (left), real part (middle)and phase (right)

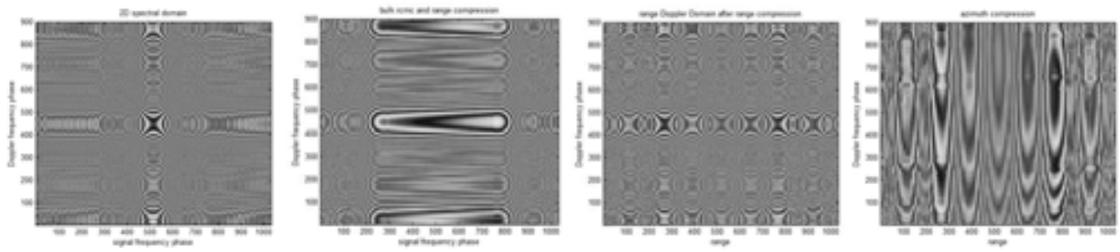


Fig. 4. Phase of spectra in range direction. RCMC. Phase of spectra after range compression. Phase of spectra in azimuth direction.

3. Image and speckle models

SAR images are affected by a noise-like characteristic called speckle that affects all coherent imaging systems and, therefore, can be observed in laser, acoustic and radar images. Basically, this usually disturbing effect is caused by random interferences, either constructive or destructive, between the electromagnetic waves which are reflected from different scatterers present in the imaged area. SAR images appear to be affected by a granular and rather strong noise named speckle. Speckle becomes visible only in the detected amplitude or intensity signal. The complex signal by itself is distorted by thermal noise and signal processing induced effects only. As a consequence of the speckle phenomenon, the interpretation of detected SAR images is highly disturbed and cannot be done with standard tools developed for non-coherent imagery. Magnitude and phase of the scatterers are statistically independent, allowing to obtain the received signal by a simple summation of the individual contributions. Interactions between scatterers are neglected. The phase of the scatterers is uniformly distributed between 0 and 2π, i.e. speckle is assumed to be fully developed.

3.1 SAR image statistics

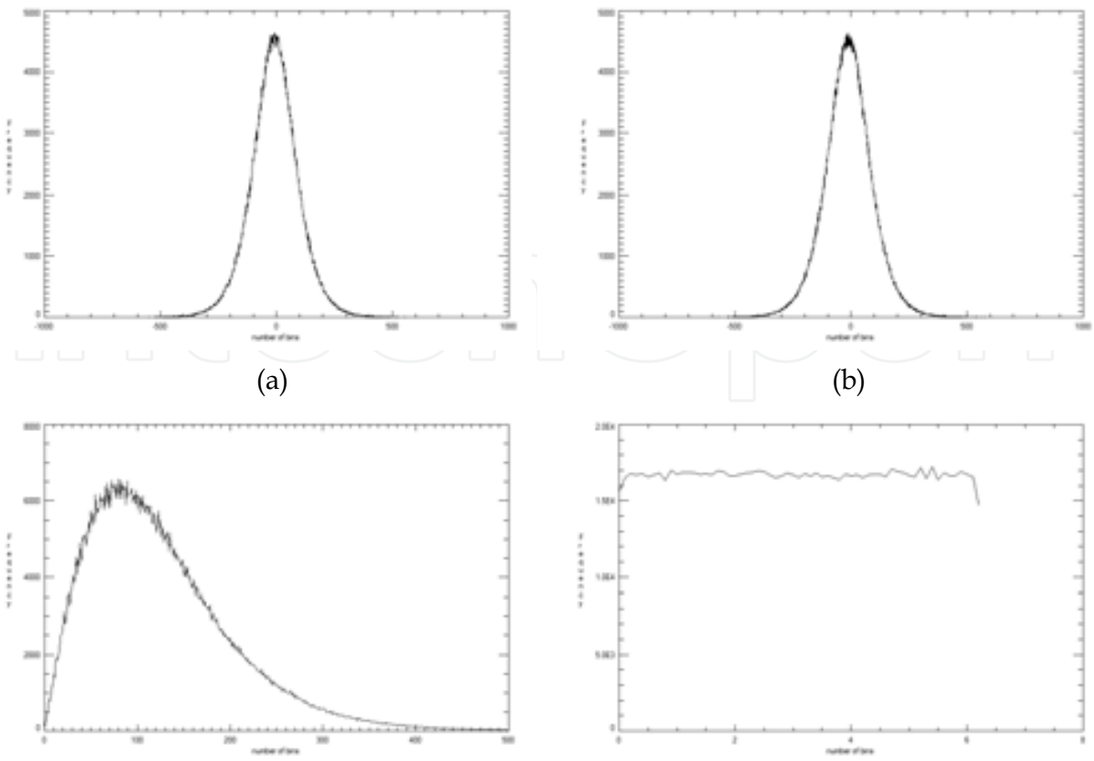
The SAR image is a complex image, where the real and imaginary part have Gaussian distribution, with zero mean and its real and theoretical distributions are shown in Fig. 5(a) and 5(b). The amplitude of the SAR image is obtained using the absolute value and can be modeled using Gamma distribution

$$p(x) = 2\left(\frac{x}{\mu}\right)^{2L-1} \frac{L^L}{\mu\Gamma(L)} \exp\left(-L\left(\frac{x}{\mu}\right)^2\right) \tag{8}$$

where L represents equivalent number of looks $L = \mu^2/\sigma^2$, μ and σ^2 represent the mean value and variance of the image, respectively. Histograms of amplitude, phase, real and imaginary part of the SAR image are shown in Figs. 5(c)-5(d), respectively.

3.2 Markov random fields

Bayesian data analysis is well suited to image interpretation in combination with appropriate prior models for the noiseless scene. The quality of the estimate, however, depends largely on the employed model and its ability to describe the image content. In this context, Markov and Gibbs random fields (MRFs and GRFs) play an important role, since



(a) (b)

(c) (d)

Fig. 5. Histograms of (a) real part, (b) imaginary part, (c) amplitude, (d) phase

they are able to statistically describe correlations, or even more generally, any kind of statistical dependence between neighboring pixels. Furthermore, they are easily applicable within the Bayesian framework. Originating from statistical physics, where they have been used for the study of phase transitions, they are now widely employed to model two-dimensional lattices, such as image data. In the beginning, the use of Markov models in image processing was limited due to the constraint of causality, but after a solution to this problem had been found, they quickly became one of the standard image processing tools.

The information of digital images is not only encapsulated in gray-values of individual pixels. More than that, images are usually composed of different regions and features with similar statistical properties, such as textures, lines and contours. As of this, several independently considered pixels usually are not significant to describe all information of a certain image region, but become important by their relations and interactions with pixels in a neighborhood. The characteristics of these local interactions between pixels, defining different regions of an image, can be modeled by a Markovian formalism, which is suitable for the envisaged framework of Bayesian data analysis. The MRF model characterize the spatial statistical dependency of 2-D data by symmetric set called neighbor set. The expression $\sum_{r\in\zeta_s} \theta_r(x_{s+r} + x_{s-r})$ represents the sum of all the distinct cliques of neighboring pixels at a specific subband. For the first order model of MRF, a sum is performed over horizontal and vertical neighboring pixels. The neighbor set for a first model order is defined as ζ = {(0,1), (0,–1)(1,0), (–1,0)} and for a second model order ζ = {(0,1), (0,–1)(1,0),

(–1,0), (1,1), (–1,–1), (1,–1), (–1,1)}. The MRF model is defined for symmetric neighbor set, therefore, if $r \in \zeta_s$ then $-r \notin \zeta_s$ and ζ is defined as $\zeta = (r : r \in \zeta_s)$ [$(-r : r \in \zeta_s)$. MRF can be described by potential functions working on a local neighborhood due to the Gibbs-Markov equivalence. In principle, there are no restrictions to the contents of these potential functions. The potentials attached to different cliques do not even have to be stationary but can vary throughout the image. For the problem of image restoration or information extraction, however, a certain number of "standard" potential functions exist.
Local interactions can be described by potentials V_c for different cliques c. These potentials are a function of the gray-values of the pixels belonging to a clique. Hence, the global energy of the whole image can be written as the sum over all potentials

$$U(x) = \sum_{c \in C} V_c(x) \tag{9}$$

In the same way, the local energy at pixel xi

$$U(x_i) = \sum_{c \in C, i \in C} V_c(x_i) \tag{10}$$

which is the sum of the potentials over all cliques that include pixel x_i. As a result, the local statistical interactions of pixels within an image can be described by an appropriate set of potential functions V_c and a corresponding clique system C.

3.3 Gauss-Markov model

Gauss-Markov model is defined by the local energy function

$$U_i(x_i) = \frac{(x_i - \mu_i)^2}{2\sigma^2}, \mu_i = \sum_{k,j \in C} \theta_{k,l}(x_{k,l} + x'_{k,l}) \tag{11}$$

Parameter $\theta_{k,l}$ represents the model vector parameter. The neighborhood configuration is encapsulated in a weighted sum over all neighboring pixels resulting in a prediction μ_i for the center pixel. Assuming some distortion of the prediction μ_i by additive Gaussian noise N_i of zero mean and variance σ^2 the corresponding conditional pdf of Gauss-Markov random fields can be written in a closed form as

$$p(x) = \frac{1}{\sqrt{2\pi\sigma^2}} \exp - \frac{(x_i - \mu_i)^2}{2\sigma^2} \tag{12}$$

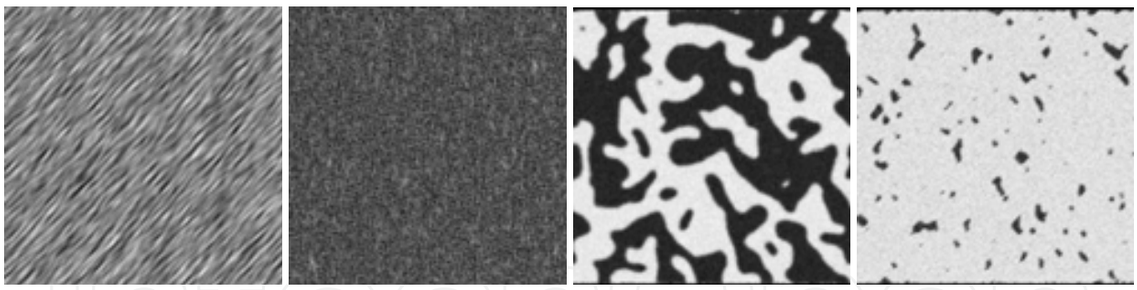
which corresponds to a linear auto-regressive process with $xi = \mu_i + n_i$, where n_i is a realization of N_i.

3.4 Auto-binomial model

An autobinomial distribution is given by

$$p(x) = \binom{G}{x} \rho^x (1-\rho)^{G-x}, \rho = \frac{1}{1+\exp(-\eta)}, \eta = a + \sum_{r \in C} \frac{b_r(x_r + x'_r)}{G} \tag{13}$$

where $\theta = a, b_{11}, b_{12}, b_{21}, b_{22}, \ldots$ represents avto-binomial model (ABM) parameters and G the maximal value in the image. A value a parameterizes the pdf of x without spatial



(a) (b) (c) (d)

Fig. 6. (a)-(b) Generated textures using GMRF. (c)-(d) Generated textures using ABM.

interactions. The number of parameters b_{ij} depends on the model order. Figs. 6(a)-6(d) show textures generated using the GMRF model and the auto-binomial model. The auto-binomial model generates more blob-like textures, while the GMRF model produces more natural and not very sharp textures.

4. Bayesian statistical modeling

Noise-free image models and noise models should be defined in order to remove noise from SAR image using Bayesian inference. The marginal distribution of wavelet subbands is well approximated by generalized Gaussian distribution. It is assumed that the image model in the wavelet domain is well approximated using general Gaussian distribution, and the noise distribution is non-stationary Gaussian noise with zero mean and locally varying variance, which is estimated from a given spatial neighborhood. We assume that the speckle noise in the wavelet domain can be approximated well using Gaussian distribution. The first level of Bayesian inference is $p(\boldsymbol{x}|\boldsymbol{y},\boldsymbol{\theta}) = \frac{p(\boldsymbol{y}|\boldsymbol{x},\boldsymbol{\theta})p(\boldsymbol{x}|\boldsymbol{\theta})}{p(\boldsymbol{y}|\boldsymbol{\theta})}$ where $\boldsymbol{y}$ is a noisy image, $\boldsymbol{x}$ is a noise-free image, $\boldsymbol{\theta}$ represents the model's parameter, $\boldsymbol{p}(\boldsymbol{y}|\boldsymbol{x}, \boldsymbol{\theta})$ denotes the conditional pdf of $\boldsymbol{y}$ over $\boldsymbol{x}$ and its so-called ***likelihood*** pdf, $\boldsymbol{p}(\boldsymbol{x}|\boldsymbol{\theta})$ denotes ***prior*** pdf and $\boldsymbol{p}(\boldsymbol{y}|\boldsymbol{\theta})$ represents ***evidence*** pdf. The $\boldsymbol{p}(\boldsymbol{y}|\boldsymbol{\theta})$ pdf does not play a role in the maximization over $\boldsymbol{x}$ and, therefore, the Maximum A Posteriori (MAP) estimator is given by $\hat{\boldsymbol{x}}(\boldsymbol{y})$ = $\text{argmax}_{\boldsymbol{x}}\, \boldsymbol{p}(\boldsymbol{y}|\boldsymbol{x}, \boldsymbol{\theta})\boldsymbol{p}(\boldsymbol{x}|\boldsymbol{\theta})$ where ***likelihood*** and ***prior*** pdf's should be defined. The MAP estimator is an optimal estimator and minimizes the cost function.

5. Maximum a posteriori despeckling using Gauss-Markov Random Field

Model based despeckling using Gauss-Markov Random Field (GMRF) model, a maximum a posteriori (MAP) estimation and evidence maximization framework was proposed in Walessa & Datcu (2000). It uses the Bayesian approach using the first level of Bayesian inference to obtain the maximum a posteriori (MAP) estimate of despeckled image. This method uses gamma pdf (8) as likelihood $p(\boldsymbol{y}|\boldsymbol{x}, \boldsymbol{\theta})$ and as prior $p(\boldsymbol{x}|\boldsymbol{\theta})$ a GMRF (12), which models and preserves textures within the image. The MAP estimate is obtained by maximizing a product $p(\boldsymbol{y}|\boldsymbol{x}, \boldsymbol{\theta})p(\boldsymbol{x}|\boldsymbol{\theta})$. is given by

$$x^4 - x^3 \sum_{j \in n} \theta_j x_j + 2L\sigma^2 x^2 - 2L\sigma^2 y^2 = 0. \tag{14}$$

The equation is solved analytically for variable x. The solution represents the approximated noise-free coefficients, which depends on texture parameter $\boldsymbol{\theta}$. The parameter estimation $\boldsymbol{\theta}$ is determined using the second level of Bayesian inference using evidence maximization. Due to the complexity of the integral it can not be computed analytically. The evidence integral consists of mutually independent process. Multidimensional probability density function is approximated by a multivariate Gaussian probability density function with Hessian matrix $\mathbf{H}$, which is centered on the maximum of a posteriori pdf. Approximation of the evidence $p(\mathbf{y}|\boldsymbol{\theta})$ is given by

$$p(\mathbf{y}|\boldsymbol{\theta}) = \int p(\mathbf{y}|\mathbf{x},\boldsymbol{\theta})p(\mathbf{x}|\boldsymbol{\theta})dx \approx \frac{(2\pi)^{\frac{m}{2}}}{\sqrt{|\mathbf{H}|}}\prod_{i=1}^{m} p(y_i|x_{i_{MAP}})p(x_{i_{MAP}}|\boldsymbol{\theta}) \tag{15}$$

where x_{iMAP} is the MAP estimate of x_i obtained using the fixed parameter vector $\boldsymbol{\theta}$ and $\mathbf{H}$ is the Hessian matrix. In order to obtain the highest evidence the set of chosen parameter $\boldsymbol{\theta}$ changes iteratively. H denotes Hessian matrix, which is the square matrix of the second order partial derivatives of a univariate function given by

$$H = -\nabla\nabla\sum_{s=1}^{N\times N}\log(p(y_s|x_s)p(x_s|\theta)) \tag{16}$$

where index s denotes the index in the 2D lattice.

$$\begin{aligned}\log p(y|\theta) &\approx 0.5\log(2\pi^{(N\times N)/2}/\sqrt{H}) + \sum_{s=1}^{N\times N}\log p(y_s|x_{s_{MAP}}) + \log p(x_{s_{MAP}}|x_{s_\eta},\theta)\\ &\approx \sum_{s=1}^{N\times N}(0.5(N\times N)\log 2\pi - \log h_{ii}) + \log p(y_s|x_{s_{MAP}}) + \log p(x_{s_{MAP}}|x_{s_\eta},\theta))\end{aligned} \tag{17}$$

$$\begin{aligned}\log p(y|\theta) = \sum_{s=1}^{N\times N}\Bigg[&0.5(N\times N)\log 2\pi - \log h_{ii}) + \log\left(2\left(\frac{y_s}{x_s}\right)^{2L-1}\frac{L^L}{x_s\Gamma(L)}\exp -L\left(\frac{y_s}{x_s}\right)^2\right)\\ &+\log\left(\frac{1}{\sqrt{2\pi\sigma^2}}\exp -\frac{(x_i-\mu_i)^2}{2\sigma^2}\right)\Bigg]\end{aligned} \tag{18}$$

$$h_{ii} \approx \left(6L\frac{y_s^2}{x_s^4} - \frac{2L}{x_s^2} + \frac{1}{\sigma^2}\left(1+|\boldsymbol{\theta}|^2\right)\right) \tag{19}$$

where h_{ii} are the main diagonal elements of the Hessian matrix H. The second derivate can be computed analytically. The final approximation is given by $|H| \approx \prod_{i=1}^{N} h_{ii}$.

The parameter $\boldsymbol{\theta}$ requires sequential computation of the MAP estimate and its evidence $p(y|\theta)$. In the first step the MAP estimate is computed using initial parameter $\boldsymbol{\theta}$. For those MAP estimates within window size of $N \times N$ the evidence is computed. One parameter θ_i is changed and the evidence is computed. If the evidence is increased, new estimate is kept,

and second parameter θ_{i+1} is changed and the evidence is computed. If the evidence decreases the parameter θ_i is unchanged. All parameters θ_i are changed until the evidence is growing. When the evidence is not changing any more, $\boldsymbol{\theta}$ represents the final solution.

6. Maximum a Posteriori despeckling using Auto-binomial Model (MAP-ABM)

A Maximum a Posteriori despeckling using Auto-binomial Model method Hebar et al. (2009) is also based on the Bayesian approach. The likelihood probability is modeled using the Gamma distribution (8) and an auto-binomial model (13) is used as a prior pdf. The auto-binomial model is discrete function, therefore, the differential is introduced to solve the MAP estimation numerically. The MAP estimate is given by

$$\frac{\Delta}{\Delta x_i}\log p(x_i \mid y_i) = \frac{\Delta}{\Delta x_i}\log\left[2\left(\frac{y_i}{x_i}\right)^{2L-1}\frac{L^L}{x_i\Gamma(L)}\exp\left(-L\left(\frac{y_i}{x_i}\right)^2\right)\right] + \frac{\Delta}{\Delta x_i}\log\left[\binom{G}{x_i}\rho^{x_i}(1-\rho)^{G-x_i}\right] \quad (20)$$

The first expression can be solved analytically. However, the second expression which represents the Auto-binomial model is solving subtracting $\log p((x_i + 1) \mid \theta_i) - \log p(x_i \mid \theta_i)$ numerically. The result is given by the zeros of

$$-2L\frac{y_i}{x_i} + 2L\frac{y_i^2}{x_i^3} + \log\left(\frac{G-x_i}{x_i+1}\right) + \log\left(\frac{\rho}{1-\rho}\right) \quad (21)$$

The MAP estimate was found using Brent's method algorithm for numerical solution of roots. In the second level of Bayesian inference, the evidence maximization was adapted to logarithm form using the Auto-binomial model. The parameter ρ in (20) depends on model parameter θ, defined in (13). The parameter $\boldsymbol{\theta}$ define ABM and it is determined using the evidence maximization approach. The evidence is given by

$$\begin{aligned}\log p(y \mid \theta) = \sum_{s=1}^{N\times N}\Big[&0.5(N\times N)\log 2\pi - \log h_{ii}\Big) \\ &+ \log\left(2\left(\frac{y_s}{x_s}\right)^{2L-1}\frac{L^L}{x_s\Gamma(L)}\exp\left(-L\left(\frac{y_s}{x_s}\right)^2\right)\right) \\ &+ \log\left(\binom{G}{x_s}\rho_s^{x_s}(1-\rho_s)^{G-x_s}\right)\Big]\end{aligned} \quad (22)$$

$$h_{ii} \approx \sum_{s=1}^{N\times N}\left(\frac{2L}{x_s^2} - 6L\frac{y_s^2}{x_s^4} - \frac{1}{G-x_s} - \frac{1}{x_s+1}\right) \quad (23)$$

The evidence maximization is very similar to the algorithm MAP-ABM. The texture parameters are changed in order to increase the evidence. The evidence shows how good the model fits to the original data. The synthetic generated data are fitted to the original data.

7. Maksimum a posteriori despeckling using generalized Gaussian-Markov Random field model

The wavelet subbands represents coarse to fine representation of the image in the terms of frequencies and spatial orientation. The reader is pointed to the literature for details regarding the wavelet transform Daubechies (1992), Chan (1995), Chui (1992). The decomposition is implemented using high and low pass filters, therefore the subbands at the high scale represents subbands with high frequencies and subbands at the low scale represents subbands with low frequencies. The time-frequency analysis can be easily done using the properties of subband decomposition. The subbands, in general, have Generalized Gaussian distribution and zero mean. The despeckling and information extraction using Bayesian inference, therefore, require models based on Gaussian distribution. The speckle within the wavelet domain is approximated using the Gaussian distribution and an image model can be approximated by the Generalized Gaussian distribution. Information extraction using GMRF can be extended using the generalized GMRF. The prior pdf $p(x)$, which has the form of a Generalized Gaussian Markov Random Field (GGMRF), is given by

$$p(x_s \mid \theta) = \frac{\nu\eta(\nu,\sigma_x)}{2\Gamma(1/\nu)} \exp\left(-\left[\eta(\nu,\sigma_x) \left| x_s - \sum_{r\in\zeta_s} \theta_r (x_{s+r} + x_{s-r}) \right| \right]^{\nu} \right) \tag{24}$$

Let σ_x and θ define the GGMRF with a neighbor set ζ_s. The parameter ν represents the shape parameters of the GGMRF. The MAP estimate using GGMRF prior and the Gaussian likelihood is given by

$$-\nu\eta(\nu,\sigma_x) \left[\eta(\nu,\sigma_x) \left| x_s - \sum_{r\in\zeta_s} \theta_r (x_{s+r} + x_{s-r}) \right| \right]^{\nu-1} \frac{y_s - x_s}{\sigma_n^2} = 0. \tag{25}$$

The variance σ_x of a noise-free image and variance of speckle noise σ_n are estimated using the results of Foucher et al. (2001):

$$\sigma_n^2 = \psi_j \mu_x^2 C_F^2 (1 + C_x^2), \quad C_x^2 = \frac{C_{Wy}^2 - \psi_j C_F^2}{\psi_j (1 + C_F^2)} \tag{26}$$

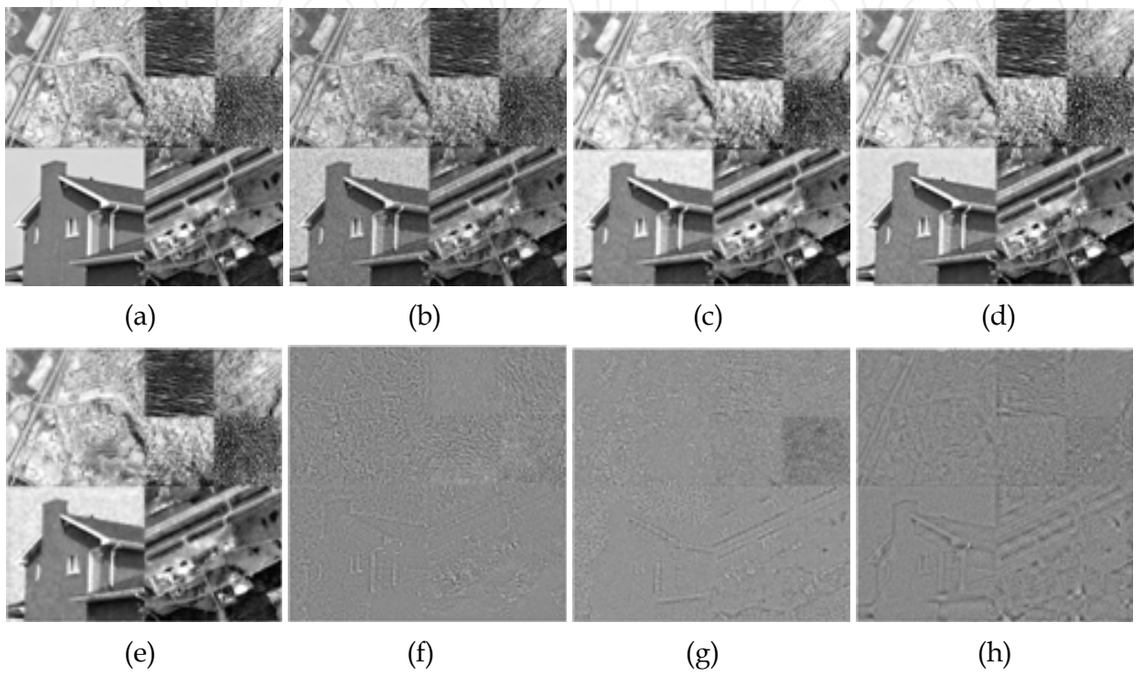
where $\mu_x = E[x]$ and C_x^2 is the normalized standard deviation of noisy wavelet coefficient is $C_{Wy} = \sigma_{Wy}/\mu_y$ and the normalized standard deviation of noise $C_F = \sqrt{1/L}$ for intensity images (where L is the number of looks) and $C_F = \sqrt{(4/\pi - 1)/L}$ for intensity images. The parameter ψ_j is defined as a product of the high pass g_k and low pass h_k filter coefficients used at j-th level of wavelet decomposition $\psi_j = \left(\sum_k h_k^2\right)^2 \left(\sum_k k_k^2\right)^{2(j-1)}$. Finally, the noise variance is given by:

$$\sigma_n^2 = \frac{C_F^2 (\psi_j \mu_y^2 + \sigma_{Wy}^2)}{1 + C_F^2} \tag{27}$$

where $\mu_y = E[y]$. The estimate for σ_n is used for all values of parameter ν. The texture parameter θ of GGMRF was estimated using minimum mean square estimate.

μ = 127.94	MAP-GMRF	MAP-ABM	MAP-GGMRF
MSE	264.34	259.31	245.45
Mean	127.84	127.86	127.89
ENL	651	539	826
Speckle	3.15	3.18	3.15
Mean($y/\hat{x}$)	0.97	0.95	0.94

Table 1. Filter Evaluation for Synthetic test images.



(a) (b) (c) (d)

(e) (f) (g) (h)

Fig. 7. (a)Original mosaic image. (b) Speckled mosaic. (c) Despeckled obtained with MAPGMRF. (d) Despeckled obtained with MAP-ABM. (e) Despeckled obtained with wavelet MAP-GGMRF. (f) Ratio image obtained with the MAP-GMRF. (g) Ratio image obtained with the MAP-ABM (h) Ratio image obtained with the wavelet MAP-GGMRF.

8. Experimental results

This section presents the efficiency of the proposed methods using objective and subjective criteria. The synthetic image, shown in Fig. 7(a), which is affected by a simulated multiplicative speckle is shown in Fig. 7(b). The MAP-GMRF and the MAP-ABM methods operate within the image domain and use the same model parameters. The window size is 15×15 the MRF order is 2 for all experiments and the step size is 1. The reconstructed image obtained with the MAP-GMRF, MAP-ABM and the MAP-GGMRF algorithms are shown in Figs. 7(c)- 7(e), respectively. The mean square error (MSE), mean of the reconstructed image, ENL of the reconstructed image, ENL of the ratio images and mean of the ratio images are reported in Table 1. The best results in the objective measurements gives the wavelet based methods, which uses the GGMRF model and is followed by the MAP-ABM and the MAP-MBD methods. All methods well reserve the mean of the reconstructed image and from the ENL results can be concluded that the MAP-GGMRF method gives the most smoothes



(a) (b) (c) (d)

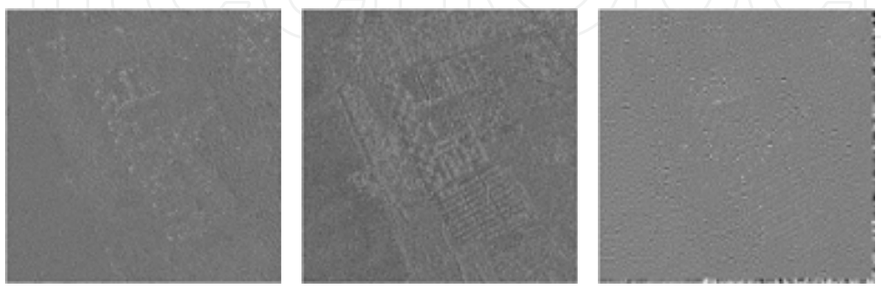
Fig. 8. (a)Original image of Cairo, Egypt (©DLR). (b) MAP-MBD despeckled (c) MAP-ABM despeckled. (d) MAP-GGMRF despeckled.

μ = 190.4	MAP-GMRF	MAP-ABM	MAP-GGMRF
Mean 190.6	190.2	190.3	
ENL	90	96	118
Speckle	4.15	4.18	4.15
Mean($y/\hat{x}$)	0.99	0.98	0.99

Table 2. Filter Evaluation for Synthetic test images.

reconstructed image and the MAP-ABM gives the most sharpest image. The ratio images shown in Figs. 7(f)-7(h), which represent the speckle, because speckle is multiplicative $y = xn$ and the ratio images represents $y/x = n$. The speckle in Table 1 represents the ENL of ratio images and should be around 3, because original images were affected by speckle with 3 ENL. All methods well estimate the speckle. The mean of speckle should be 1 and all presented methods well estimate the speckle.

Presented methods were tested using the real SAR image of Cairo, Egyipt, provided by the TerraSAR-X satellite. The resolution is 1.1 m in azimuth and 0.86 m in range. It was acquired using 300 MHz chirp. The original image is shown in Fig. 8(a) and despeckled using GMRF, ABM and GGMRF models on Figs. 8(b)-8(d). The MAP-ABM method gives very good results using, because structures are good modeled, speckle well removed and the mean of the reconstructed image is preserved well, as reported in Table 2. The MAP-GMRF method well estimates speckle, but introduces GMRF based structures, which appear, as inability of the model to adapt to the real textures. The MAP-GGMRF well remove speckle and models



(a) (b) (c)

Fig. 9. (a)Ratio image obtained with the MAP-GMRF. (b) Ratio image obtained with the MAPABM(c) Ratio image obtained with the wavelet MAP-GGMRF.

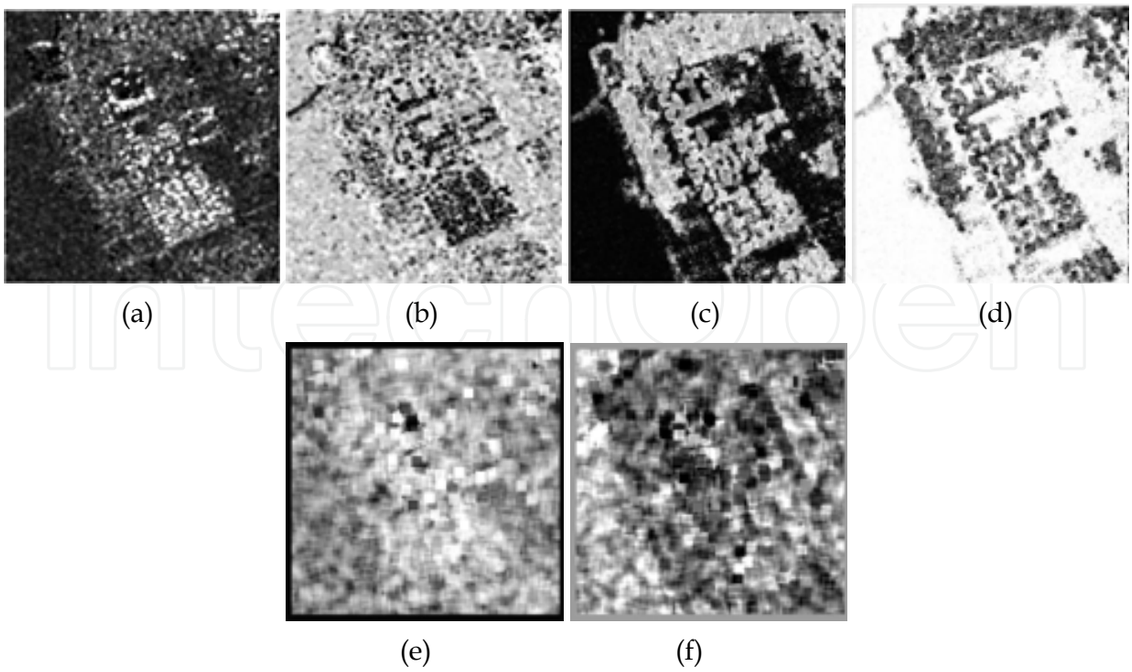


Fig. 10. Horizontal (HH) and vertical (VV) textural parameters (a)HH, MAP-GMRF. (b) VV, MAP-GMRF. (c) HH, MAP-ABM. (d) VV, MAP-GMRF. (d) HH, MAP-GGMRF. (e) VV, MAPGGMRF.

textures in the real-SAR image. Figs. 9(a)-9(c) show the ratio images of real SAR images. The speckle is well estimated with all presented methods.

The MRF based methods are able to extract features parameters. In this case the texture can be extracted using texture models. The texture parameters obtained with the GMRF, ABM and GGMRF models are shown in Figs. 10(a)-10(f), where the horizontal and vertical cliques are shown. The ABM model well models homogeneous and heterogeneous regions, as well it separates different kind of textures, as show the ABM's texture parameters on Figs. 10(c)-10(d). The GMRF model is not as efficient as the ABM model in modeling real textures, but it is still able to model homogeneous and heterogeneous regions and the parameters estimated with the GMRF model are shown in Figs. 10(a)-10(b). The wavelet based method has difficulties in modeling textures. This can be the consequence of the linear model used for the texture parameter estimation. The texture parameters obtained with the GGMRF model are shown in Fig. 10(e)-10(f).

The computational efficiency of the proposed methods were tested on real SAR image with 1024 ×1024 pixels and the execution times were 414, 560 and 103 seconds for MAP-GMRF, MAP-ABM and MAP-GGMRF methods.

9. Conclusion

Presented methods in this paper are based on Markov Random Fields. The efficiency of two methods, which work within the image domain and the wavelet based method is compared. The wavelet-based method gives good results in the objective measurements on simulated data, well preforms in the terms of despeckling, but its ability of information extraction in very poor. The ABM in GMRF based methods well despeckles the real and simulated data

and the ABM gives very good results using real SAR data. The ABM has better ability to separate blob-like textures, which occur in the real SAR images for city areas. The GMRF model is more appropriate for the natural textures.

10. References

Argenti, F., Bianchi, T. & Alparone, L. (2006). Multiresolution map despeckling of sar images based on locally adaptive generalized gaussian pdf modeling, *IEEE Transaction on Image Processing* 15: 3385–3399.

Arulampalan, S., M, Maskell, S., N., G. & Clap, T. (2002). A tutorial on particle filters for online nonlinear/non-gaussian bayesian tracking, *IEEE Transaction on Signal Processing* 50: 174–188.

Chan, Y. T. (1995). *Wavelet Basics*, Kulwer Academic Publishers, Norwell, Massachussetta, USA.

Chui, C. K. (1992). *Wavelets: A Tutorial in Theory and Applications*, Academic Press, San Diego, USA.

Chuna, A. L. d., Zhou, J. & Do, M. N. (2006). The nonsubsampled contourlet transform: Theory, design,and application, *IEEE Transaction on Image Processing* 15: 3089–3101.

Dai, M., Peng, C., Chan, A. & Loguinov, D. (2004). Multiresolution map despeckling of sar images based on locally adaptive generalized gaussian pdf modeling, *IEEE Transaction on Geoscience and Remote Sensing* 42: 1642–1648.

Daubechies, I. (1992). *Ten Lectures onWavelets*, Society for industrial and applied mathematics, Philadelphia, Pennsylvania.

Foucher, S., Benie, G. B. & Boucher, J.-M. (2001). Multiscale map filtering of sar images, *IEEE Tran. Image Processing* 10(1): 49–60.

Gleich, D. & Datcu, M. (2007).Wavelet-based despeckling of SAR images using Gauss-Markov random fields, *IEEE Transaction on Geoscience and Remote Sensing* 45(12): 4127–4143.

Hebar, M., Gleich, D. & Cucej, Z. (2009). Autobinomial model for sar image despeckling and information extraction, *IEEE Transaction on Geoscience and Remote Sensing* 47(8): 2818– 2835.

Li, Y.-q., He, M.-y. & Gang, X.-f. (2006). Ieee conference on signal processing, *A New Adaptive Algorithm for Despeckling of SAR images Based on Contourlet Transform*.

Sivia, D. S. (1996). *Data Analysis: A Bayesian Tutorial*, Oxford, U.K., Clarendon.

Sveinsson, J. R. & Benediktsson, J. A. (2007). Ieee international conference on geoscience and remote sensing, *Speckle Reduction of SAR Images in the Bandelet Domain*.

Walessa, M. & Datcu, M. (2000). Model-based despeckling and information extraction from sar images, *IEEE Transaction on Geoscience and Remote Sensing* 38: 2258–2269.



New Trends in Technologies: Control, Management, Computational Intelligence and Network Systems
Edited by Meng Joo Er

ISBN 978-953-307-213-5
Hard cover, 438 pages
Publisher Sciyo
Published online 02, November, 2010
Published in print edition November, 2010

The grandest accomplishments of engineering took place in the twentieth century. The widespread development and distribution of electricity and clean water, automobiles and airplanes, radio and television, spacecraft and lasers, antibiotics and medical imaging, computers and the Internet are just some of the highlights from a century in which engineering revolutionized and improved virtually every aspect of human life. In this book, the authors provide a glimpse of the new trends of technologies pertaining to control, management, computational intelligence and network systems.

How to reference
In order to correctly reference this scholarly work, feel free to copy and paste the following:

Dusan Gleich and Zarko Cucej (2010). Recent Advances in Synthetic Aperture Radar Enhancement and Information Extraction, New Trends in Technologies: Control, Management, Computational Intelligence and Network Systems, Meng Joo Er (Ed.), ISBN: 978-953-307-213-5, InTech, Available from: http://www.intechopen.com/books/new-trends-in-technologies--control--management--computational-intelligence-and-network-systems/recent-advances-in-synthetic-aperture-radar-enhancement-and-information-extraction

INTECH
open science | open minds

InTech Europe
University Campus STeP Ri
Slavka Krautzeka 83/A
51000 Rijeka, Croatia
Phone: +385 (51) 770 447
Fax: +385 (51) 686 166
www.intechopen.com

InTech China
Unit 405, Office Block, Hotel Equatorial Shanghai
No.65, Yan An Road (West), Shanghai, 200040, China
中国上海市延安西路65号上海国际贵都大饭店办公楼405单元
Phone: +86-21-62489820
Fax: +86-21-62489821

© 2010 The Author(s). Licensee IntechOpen. This chapter is distributed under the terms of the Creative Commons Attribution-NonCommercial-ShareAlike-3.0 License, which permits use, distribution and reproduction for non-commercial purposes, provided the original is properly cited and derivative works building on this content are distributed under the same license.

IntechOpen

IntechOpen